

# ***N*-body simulation of planetary formation through pebble accretion in a radially structured protoplanetary disk**

**Tenri JINNO,<sup>1,\*</sup> Takayuki R. SAITO<sup>1,\*</sup> Yota ISHIGAKI,<sup>2,\*</sup> and Junichiro MAKINO<sup>1,\*</sup>**

<sup>1</sup>Department of Planetology, Graduate School of Science, Kobe University, 1-1 Rokkodai-cho, Nada-ku, Kobe, Hyogo 657-8501, Japan

<sup>2</sup>Department of Solar System Science, Institute of Space and Astronautical Science, Japan Aerospace Exploration Agency

\*E-mail: 223s415s@gsuite.kobe-u.ac.jp, saitoh@people.kobe-u.ac.jp, ishigaki@alumni.u-tokyo.ac.jp, jmakino@people.kobe-u.ac.jp

Received 2023 May 31; Accepted 2023 August 2

## **Abstract**

In the conventional theory of planet formation, it is assumed that protoplanetary disks are axisymmetric and have a smooth radial profile. However, recent radio observations of protoplanetary disks have revealed that many of them have complex radial structures. In this study, we perform a series of *N*-body simulations to investigate how planets are formed in protoplanetary disks with radial structures. For this purpose, we consider the effect of continuous pebble accretion onto the discontinuity boundary within the terrestrial planet-forming region ( $\sim 0.6$  AU). We found that protoplanets grow efficiently at the discontinuity boundary, reaching the Earth mass within  $\sim 10^4$  years. We confirmed that giant collisions of protoplanets occur universally in our model. Moreover, we found that multiple planet-sized bodies form at regular intervals in the vicinity of the discontinuity boundary. These results indicate the possibility of the formation of solar system-like planetary systems in radially structured protoplanetary disks.

**Key words:** methods: numerical — planets and satellites: formation — planets and satellites: terrestrial planets

## **1 Introduction**

One of the pioneering studies of planetary formation theory was conducted by Chushiro Hayashi's group at Kyoto University (Hayashi 1981; Hayashi et al. 1985). In their scenario, the planetary formation process starts from a disk that is stable against self-gravity. This disk is assumed to have a dust component consistent with the current mass of planets, and the dust-gas ratio comes from the solar abundance (the Minimum-Mass Solar Nebula model, MMSN). First, dust condenses to the midplane of the disk. Then, planetesimals are formed through the gravitational insta-

bility of dust. The planetesimals grow through mutual collisions to form planets. Furthermore, they showed that when the mass of a protoplanet reaches a certain critical value ( $\simeq 10M_{\oplus}$ ), disk gas flows into the planet, forming a gas giant (Mizuno 1980). Since this model successfully described the sequence of terrestrial planets, gas giants, and icy planets, it came to be regarded as the standard theory of planet formation, even though many difficulties were known.

Some of the most critical problems have been resolved. For example, the problem of the formation time of Jupiter has been resolved by the realization that planetesimals

grow through the runaway process (Wetherill & Stewart 1989; Ida & Makino 1993; Kokubo & Ida 1996). However, several problems remain unresolved, including planet migration, the occurrence of magneto-rotational instability, and the diversity of observed protoplanetary disks. In the following, we outline these problems.

First, it has been found that protoplanets that have grown to the size of Mars experience the Type I migration and drift toward the Sun due to gravitational interaction with the gas disk (Ward 1986; Tanaka et al. 2002). In the MMSN disk, the Type I migration timescale of Mars-size planets at 1 AU is estimated as  $1 \times 10^6$  yr. The orbital distribution of the planets after migration due to the Type I effect cannot reproduce the orbital distribution of the solar system (Ida & Lin 2008).

Second, the occurrence of the magneto-rotational instabilities (MRI) in accretion disks was found in the early 1990s (Balbus & Hawley 1991), indicating that the structure of protoplanetary disks is much more complex than what was assumed in the standard theory. More recently, it has been pointed out that in many protoplanetary disks, turbulence originating from MRI does not occur or is suppressed in certain radial ranges (Bai & Stone 2013). This region is called the dead zone. This dead zone is considered to be a laminar structure sandwiched by two turbulent outer layers (Armitage 2011), since cosmic rays can keep the ionization ratio of the outer layers high enough for MRI to occur. In this turbulent region, the existence of magnetic disk winds has been theoretically predicted. This disk wind is expected to be the mechanism to remove the angular momentum from protoplanetary disks (Suzuki et al. 2016). Planetary system formation in protoplanetary disks with dead zone and magnetic disk winds is now being actively studied (e.g., Lyra et al. 2009; Matsumura et al. 2021).

Third, recent observations using Atacama Large Millimeter/sub-millimeter Array (ALMA) have revealed the presence of non-axisymmetric dust distributions and ring-like structures within protoplanetary disks (e.g., Muto et al. 2015; Andrews et al. 2018). The standard theory, which assumes a smooth disk structure, cannot explain these sub-structures observed in protoplanetary disks or the planet formation process within the structured disk.

In recent years, pebble accretion has attracted attention (Birnstiel et al. 2012; Lambrechts & Johansen 2012; 2014). Smaller pebbles, typically on the order of cm-size, are instrumental in driving pebble accretion. They efficiently migrate inward through hydrodynamic drag (Weidenschilling 1977; Nakagawa et al. 1986). These pebbles may accumulate at the boundary between the dead zone and the inner turbulent zone where a pressure bump

exists (Kato et al. 2010). In addition, it has been pointed out that in the dead zone, the radial velocity of pebbles may be slowed down by pebble-gas back-reaction, potentially resulting in a runaway pile-up of pebbles (Hyodo et al. 2021; 2022). In either case, the supply of pebbles to the core feeding region may lead to efficient planet formation.

As we have seen above, the standard theory has many problems, and many ideas have been proposed to solve them. In this study, we constructed a disk model that incorporates ideas to overcome these problems in a consistent manner as a whole and performed *N*-body simulations to study the formation of terrestrial planets. It should be noted that, even though we start with a specific disk model inspired by that of Ebisuzaki & Imaeda (2017) (hereafter EI17), our scenario can be applied to any disk model which has the inner cutoff at around 1AU (e.g., Suzuki et al. 2016).

*N*-body simulations in which the pebble accretion process to planetary cores is taken into account have been performed in several studies (e.g., Matsumura et al. 2017; 2021, Lau et al. 2022 and Jiang & Ormel 2023). The first two studies have simulated the growth of planetary embryos, assuming that they grow through pebble accretion. The growth rate of embryos is given by the analytic function. This implies that in their model how and where the embryos are formed and how they grow are model assumptions. The latter two studies have investigated the formation and evolution of planetesimals, taking into account pebble accretion in the rings induced by permanent pressure bumps. They determined the locations of the pressure bump, motivated by the observed ring structures (e.g., Andrews et al. 2018). Therefore, both studies focus on planet formation at pressure bumps located at distances of 10 AU and 75 AU from the central star, which are outside the region where terrestrial planets form.

In addition to the studies discussed above, Coleman & Nelson (2016) have investigated the process of gas giant formation within protoplanetary disks that contain multiple ring-like structures using *N*-body simulations. They include spatially and temporally varying viscous stresses within a limited radius, allowing for the reproduction of the formation and decay of pressure-induced rings within the disk. However, it should be noted that their research does not encompass the formation of pressure-induced rings within the region where terrestrial planet formation occurs. There have been studies that utilize planet population synthesis calculations that account for planetary growth by core accretion and planetary migration by Type-I and Type-II migrations (e.g., Alessi & Pudritz 2018).

We intend to study the formation and growth of ter-

restrial planets from infalling pebbles, which are trapped at the inner boundary of the dead zone ( $\sim 0.6$  AU). We model pebbles as  $N$ -body particles and solve their interactions directly through large-scale  $N$ -body simulations with up to 1 million particles.

This paper is organized as follows. In section 2, we present our model for the structure of the protoplanetary disk, the dust growth, and the growth of planets. The last part is modeled by  $N$ -body simulation. In section 3, we present the results of  $N$ -body simulations and show how pebbles grow to planets size at the inner boundary of the disk. We also show the results of  $N$ -body simulations on disk models with various gas-dust ratios and particle numbers. In section 4, we overview the growth scenario of planets in our model and compare it with other models. In section 5, we make concluding remarks.

## 2 Model and Numerical Method

### 2.1 Overview of Our Model

The aim of our study is to investigate how planet formation proceeds when we take into account the continuous pebble accretion to discontinuous boundaries of the protoplanetary disk. To do so, we constructed a protoplanetary disk model with a discontinuous structure and a model for the growth and migration of dust particles in it. By combining these two models, we obtain the time-varying mass inflow rate at the disk inner boundary. We conducted a series of  $N$ -body simulations of planetary growth under this inflow rate.

We constructed a gas disk model following EI17. The outer and inner regions of the disk are turbulent while the intermediate region is non-turbulent (i.e., the dead zone). Such a disk with a dead zone seems to be the natural outcome of the theoretical model of protoplanetary disks (Armitage 2011). In such a disk, a pressure bump forms at the boundary of the dead zone, causing dust particles to accumulate (Kato et al. 2010; Chatterjee & Tan 2014). For simplicity, we assume that our gas disk is a stationary one-dimensional  $\alpha$  disk (Shakura & Sunyaev 1973).

We also constructed a model for the growth and migration of the dust particles in the gas disk to determine the mass inflow rate at the inner boundary of the dead zone (Johansen & Lambrechts 2017). This is how we express pebble accretion.

Using these models, we determine the mass inflow rate at the inner boundary of the dead zone. We construct the initial condition for our  $N$ -body simulation to realize this inflow rate (see section 2.4 for details). We conducted  $N$ -body simulations with initial particle numbers ranging

from  $6 \times 10^4$  to  $10^6$ .

### 2.2 The gas disk

Here we present our protoplanetary disk model surrounding a solar mass star.

#### 2.2.1 The surface density of the gas disk

Our disk model is one-dimensional. The time evolution of the surface density of the gas disk  $\Sigma$  is given by the continuity equation

$$\frac{\partial \Sigma}{\partial t} = \frac{1}{2\pi r} \frac{\partial \dot{M}}{\partial r}, \quad (1)$$

where the mass accretion rate  $\dot{M}$  (positive for inward accretion) is defined using the gas radial velocity  $v_r$  as:

$$\dot{M} = -2\pi r \Sigma v_r. \quad (2)$$

We neglect the time evolution of the disk and regard it as in a steady state. In this case, we can rewrite eq.(1) as

$$\frac{\partial \dot{M}}{\partial r} = 0. \quad (3)$$

Using eqs.(2), (3), and the azimuthal direction component of the fluid equation of motion

$$\Sigma v_r r \frac{\partial}{\partial r} (r^2 \Omega) = \frac{\partial}{\partial r} \left( r^3 \Sigma \nu \frac{\partial \Omega}{\partial r} \right), \quad (4)$$

we obtain

$$\begin{aligned} \dot{M} &= -2\pi r \Sigma v_r, \\ &= 6\pi r^{1/2} \frac{\partial}{\partial r} (\Sigma \nu r^{1/2}) = \text{const}, \end{aligned} \quad (5)$$

where  $\nu$  and  $\Omega$  are the disk viscosity and the Keplerian orbital frequency. Here  $\Omega$  is given as

$$\Omega = \left( \frac{GM_*}{r^3} \right)^{1/2} = 2.0 \times 10^{-7} \left( \frac{r}{\text{AU}} \right)^{-3/2} \text{ s}^{-1}, \quad (6)$$

where  $G$  is the gravitational constant and  $M_*$  is the mass of the central star. We set  $M_* = 1M_\odot$ . Integrating eq.(5) with respect to  $r$ , we obtain

$$\Sigma = \frac{\dot{M}}{3\pi\nu}. \quad (7)$$

We assume that the disk is an  $\alpha$ -disk so that the viscosity can be expressed by

$$\nu = \alpha c_s H, \quad (8)$$

where  $\alpha$  is the viscous parameter,  $c_s$  is the sound velocity, and  $H$  is the scale height of the disk. The functional forms of  $c_s$  and  $H$  are given as follows:

$$c_s = \left( \frac{k_B T_m}{\mu m_H} \right)^{1/2} = 1.0 \times 10^5 \left( \frac{T_m}{280 \text{ K}} \right)^{1/2} \text{ cm s}^{-1}, \quad (9)$$

$$H = \frac{c_s}{\Omega} = 5.0 \times 10^{11} \left( \frac{T_m}{280 \text{ K}} \right)^{1/2} \left( \frac{r}{\text{AU}} \right)^{3/2} \text{ cm}, \quad (10)$$

where  $T_m$  is the mid-plane temperature of the gas disk (see section 2.2.2),  $k_B$  is the Boltzmann constant,  $\mu = 2.34$  is the mean molecular weight of the gas and  $m_H$  is the mass of a hydrogen atom.

The value of the viscous parameter  $\alpha$  is different for turbulent and non-turbulent regions (Armitage 2020). Here we adopt the following values

$$\alpha = \begin{cases} \alpha_{\text{act}} = 1.0 \times 10^{-2} & \text{for turbulent region} \\ \alpha_{\text{inact}} = \gamma \alpha_{\text{act}} = 1.0 \times 10^{-2.5} & \text{for non-turbulent region.} \end{cases} \quad (11)$$

where  $\alpha_{\text{act}}$  is determined using the result of numerical MHD simulations of planetary disks (Davis et al. 2010). We assumed the reduction factor of turbulent  $\gamma$  to be  $\gamma = 10^{-0.5} \simeq 0.316$  for the entire non-turbulent region, though  $\gamma$  has not been constrained well yet.

EI17 solved the steady-state equation of the disk to obtain the locations of the inner and outer boundaries of the dead zone. Here, we adopt their numerical results to determine the location of the boundaries as a function of the mass accretion rate  $\dot{M}$ . We employed single power law forms to fit the numerical results and these are:

$$r_{\text{in}} = 1.1 \times 10^3 \dot{M}^{0.47} \text{ AU}, \quad (12)$$

$$r_{\text{out}} = 6.6 \times 10^5 \dot{M}^{0.62} \text{ AU}, \quad (13)$$

where  $r_{\text{in}}$  and  $r_{\text{out}}$  represent the inner and outer boundaries of the dead zone, respectively. The region between  $r_{\text{in}}$  and  $r_{\text{out}}$  is MRI inactive and  $\alpha = \alpha_{\text{inact}}$  for this region. Other regions are MRI active and  $\alpha = \alpha_{\text{act}}$  for these regions. These coefficients and power law indexes are determined to reproduce EI17 results:  $r_{\text{in}} = 1 \text{ AU}$  and  $r_{\text{out}} = 60 \text{ AU}$  for  $\dot{M} = 10^{-6.5} M_\odot/\text{yr}$  and  $r_{\text{in}} = 0.2 \text{ AU}$  and  $r_{\text{out}} = 7 \text{ AU}$  for  $\dot{M} = 10^{-8.0} M_\odot/\text{yr}$ .

## 2.2.2 The mid-plane temperature of the gas disk

In order to determine  $\Sigma$ , we need the temperature of the disk. Following Hubeny (1990), we use the following equation for the mid-plane temperature  $T_m$ :

$$T_m^4 = \left( \frac{3\dot{M}\Omega^2}{8\pi\sigma} \right) \left( \frac{3}{8} \frac{\alpha}{\alpha_{\text{act}}} \frac{\kappa\Sigma}{2} + \frac{\sqrt{3}}{4} \right) + T_{\text{irr}}^4, \quad (14)$$

where  $\sigma$  is the Stefan-Boltzmann constant,  $\alpha_{\text{act}}$  is the viscous parameter for the MRI active state,  $\kappa$  is the opacity of the gas disk, and  $T_{\text{irr}}$  is the irradiation temperature due to the central star. We adopt the opacity of the gas disk  $\kappa$  (in unit of  $\text{cm}^2/\text{g}$ ) from Stepinski (1998):

$$\kappa = \begin{cases} 2 \times 10^{-4} T_m^2 & T_m < 150 \text{ K} \\ 1.15 \times 10^{18} T_m^{-8} & 150 \text{ K} \leq T_m < 180 \text{ K} \\ 2.13 \times 10^{-2} T_m^{3/4} & 180 \text{ K} \leq T_m < 1380 \text{ K} \\ 4.38 \times 10^{44} T_m^{-14} & T_m \geq 1380 \text{ K} \end{cases} \quad (15)$$

The irradiation temperature  $T_{\text{irr}}$  is given by Coleman & Nelson (2014):

$$T_{\text{irr}}^4 = \frac{1}{2} (1 - \epsilon) T_*^4 \left( \frac{R_*}{r} \right)^2 \left[ \frac{4}{3\pi} \left( \frac{R_*}{r} \right) + \frac{2}{7} \frac{H}{r} \right], \quad (16)$$

where  $\epsilon$  is the albedo of the disk,  $T_*$  and  $R_*$  are the temperature and radius of the central star. Following Coleman & Nelson (2014), we set values of  $\epsilon$ ,  $T_*$  and  $R_*$  to be 0.5, 4000 K and  $3R_\odot$  respectively.

## 2.2.3 The overall structure of the gas disk

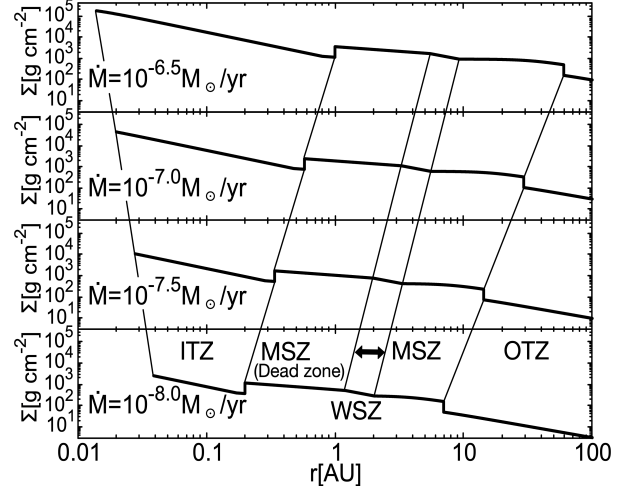


**Fig. 1.** The radial profile of the surface density of the gas disk with different mass accretion rates ( $\dot{M} = 10^{-8.0} - 10^{-6.5} M_\odot/\text{yr}$ ).

Fig. 1 shows the surface density profile of the gas disk for four different mass accretion rates ranging from  $10^{-8.0} M_\odot/\text{yr}$  to  $10^{-6.5} M_\odot/\text{yr}$ . For all cases, there are two discontinuous boundaries in the surface density. We call them inner dead zone boundary (IDB) and outer dead zone boundary (ODB). As we have discussed in section 2.2.1, we used the result of the 1D disk calculation of EI17 to determine the location of these boundaries.

We call the inner and outer turbulent zones inner turbulent zone (ITZ) and outer turbulent zone (OTZ) respectively. The non-turbulent zone, which we call the MRI-suppressed zone (MSZ) exists between ITZ and OTZ. Slight slope changes are seen in MSZ. This reflects the change of opacity in the gas disk due to the sublimation of ice at temperature 180–150 K [eq.(15)]. We call this region the water sublimation zone (WSZ).

Near the central star, the gas disk is truncated by the magnetic field of the central star. The radius of disconnection is called the Alfvén radius  $r_A$ , which is the radius where the magnetic pressure of the central star is balanced by the gas pressure of the accreting gas disk. Since  $r_A$  is proportional to  $\dot{M}^{-2/7}$ ,  $r_A$  moves outward as the mass accretion rate decreases.

The region of interest in this study is the vicinity of IDB, where a discontinuity in the gas surface density profile is created by the change in the value of  $\alpha$ . This surface density gap creates a pressure bump in IDB. It is expected that planets form efficiently as dust that accretes from the outer regions gets trapped near IDB due to the pressure bump (Kato et al. 2010; Chatterjee & Tan 2014).

### 2.3 Evolution of dust particles in the gas disk

In this subsection, we first present the physical background of the growth and migration of the dust particles and describe the assumption made in our model (section 2.3.1). Then, in section 2.3.2 and 2.3.3, we describe our model for the growth and migration of the dust particle within the disk presented in the previous subsection.

#### 2.3.1 Physical background and modeling assumption of dust particles growth and migration

Dust particles outside of IDB ( $r > r_{\text{in}}$ ) grow via collisions with other dust particles. As dust particles continue to grow through mutual collisions, they drift inward due to the effect of the gas drag (Adachi et al. 1976). This inward migration continues until dust particles reach IDB, where the presence of pressure bump halts their inward migration (Kato et al. 2010; Chatterjee & Tan 2014).

We solve the growth and migration of dust particles simultaneously to determine the mass inflow rate onto IDB. The radial migration timescale for dust particles ranging from  $\mu\text{m}$  to  $\sim\text{cm}$  in size (i.e., with a mass of  $\sim 10^4 \text{ g}$  or less) is significantly longer than the growth timescale (see section 2.3.3). Thus, in our model, we initially approximate that dust particles grow through mutual collisions in situ, and once they have grown to critical mass  $m_c$ , they subsequently drift towards the Sun due to the effect of the gas drag. This approximation is similar to the idea proposed by Lambrechts & Johansen (2014). They proposed a pebble flux calculation model based on the idea that all the dust grows to the drift limits at a certain radius, decoupled from the gas, and drifts inwards.

Our approximation for dust particle growth and migration allows us to calculate the growth of dust particles and the drift of particles separately. Thus, we can define the mass accretion timescale onto IDB,  $t_{\text{acc}}$ , as the sum of the time it takes for a dust particle to grow to  $m_c$  and its radial migration timescale (see Appendix 1 for details).

#### 2.3.2 The growth rate of dust particles

In our model, dust particles grow via collisions with other dust particles. The rate of dust particle growth is given by

$$\frac{dm_p}{dt} = \dot{m}_p = \pi a_p^2 \rho_p v_{\text{rel,pp}} \left( 1 + \frac{2Gm_p}{a_p v_{\text{rel,pp}}^2} \right), \quad (17)$$

where  $m_p$  is the particle mass,  $a_p$  is the dust particle radius,  $\rho_p$  is the dust particle density at the particle scale height, and  $v_{\text{rel,pp}}$  is the particle-particle relative velocity. By integrating eq.(17), we determine the evolution of  $m_p$ . In the following, we describe how we determine the parameters in eq.(17).

The particle radius  $a_p$  in eq.(17) is given by

$$a_p = \left( \frac{3m_p}{4\pi\rho_i} \right)^{1/3}. \quad (18)$$

Since we consider the dust particles inside WSZ, here we use the dust particle internal density  $\rho_i = 2 \text{ g cm}^{-3}$  which is appropriate for carbonaceous material.

The dust particle density at the particle scale height is given by

$$\rho_p = \frac{\bar{f}\Sigma}{\sqrt{2\pi}z_p} \exp\left(-\frac{1}{2}\right), \quad (19)$$

where  $\bar{f}$  is the dust-to-gas fraction and  $z_p$  is the scale height of the dust particles. Here, we adopt  $\bar{f} = \bar{f}_{\text{MMSN}} = 2.5 \times 10^{-3}$  (for  $\text{IDB} < r < \text{WSZ}$ ) where  $\bar{f} = \bar{f}_{\text{MMSN}}$  is what assumed in Hayashi et al. (1985).

The scale height of dust particles  $z_p$  is given by EI17 as:

$$\frac{dz_p}{dt} = -v_{zp} \quad \text{for } z_p > H_p, \quad (20)$$

$$z_p = H_p \quad \text{for } z_p < H_p, \quad (21)$$

where  $H_p$  and  $v_{zp}$  are the particle scale height in equilibrium and the particle settling velocity. In our model, we adopt the scale height of the gas disk  $H$  as the initial value of  $z_p$ . The particle scale height in equilibrium  $H_p$  is given by Youdin & Johansen (2007):

$$H_p = \left( 1 + \frac{\Omega t_s}{\alpha_D} \right)^{-\frac{1}{2}} \left( 1 + \frac{\Omega t_s}{\Omega t_s + 1} \right)^{-\frac{1}{2}} H, \quad (22)$$

where  $\Omega$  is the Keplerian orbital frequency given by eq.(6),  $t_s$  is the particle stopping time, and  $\alpha_D$  is the effective viscous parameter of the gas disk in the region where dust particles exist. Following Sato et al. (2016), we use the equation for the particle stopping time  $t_s$ :

$$t_s = \begin{cases} \frac{4\rho_i a_p^2}{9\rho_g v_{\text{th}} \lambda} & \text{for } (a_p > \frac{9}{4}\lambda), \\ \frac{\rho_i a_p}{\rho_g v_{\text{th}}} & \text{for } (a_p \leq \frac{9}{4}\lambda), \end{cases} \quad (23)$$

where  $\rho_g$ ,  $v_{\text{th}}$  and  $\lambda$  are the gas density, the thermal velocity, and the mean free path of the gas molecule at given  $r$  and  $z$ . These parameters are given as follows:

$$\rho_g = \frac{\Sigma}{\sqrt{2\pi}H} \exp\left(-\frac{z^2}{2H^2}\right), \quad (24)$$

$$v_{\text{th}} = \sqrt{\frac{8k_B T_m}{\pi\mu}}, \quad (25)$$

$$\lambda = \frac{\mu}{\sigma_{\text{col}} \rho_g}. \quad (26)$$

Here,  $\sigma_{\text{col}} = 2.0 \times 10^{-15} \text{ cm}^2$  is the molecular collision cross-section. The particle stopping time is expressed in terms of the dimensionless Stokes number as

$$\text{St} \equiv \Omega t_s. \quad (27)$$

We, hereafter use St instead of  $\Omega t_s$ . The particle settling velocity in eq.(20) is given by

$$v_{z\text{p}} = \frac{\text{St}}{\text{St} + 1} z_p \Omega. \quad (28)$$

The particle-particle relative velocity is given by Ormel & Cuzzi (2007) as:

$$v_{\text{rel,pp}} = \sqrt{v_B^2 + v_{r\text{pp}}^2 + v_{\phi\text{pp}}^2 + v_{z\text{pp}}^2 + v_{\text{turb,pp}}^2}, \quad (29)$$

$$v_B = \sqrt{\frac{16 k_B T_m}{\pi m_p}}, \quad (30)$$

$$v_{r\text{pp}} = \left( \frac{2\text{St}}{1 + (\text{St})^2} - \frac{\text{St}}{1 + (0.5\text{St})^2} \right) \eta r \Omega, \quad (31)$$

$$v_{\phi\text{pp}} = - \left( \frac{(\text{St})^2}{1 + (\text{St})^2} - \frac{(0.5\text{St})^2}{1 + (0.5\text{St})^2} \right) \eta r \Omega, \quad (32)$$

$$v_{z\text{pp}} = \left( \frac{\text{St}}{1 + \text{St}} - \frac{0.5\text{St}}{1 + 0.5\text{St}} \right) z_p \Omega, \quad (33)$$

$$v_{\text{turb,pp}} = \sqrt{\alpha_D c_s} \times \begin{cases} \text{Re}^{1/4} \Omega |0.5t_s| & \text{for } \text{St} < 8\text{Re}^{-1/2} \\ \sqrt{2\text{St}} & \text{for } 8\text{Re}^{-1/2} \leq \text{St} < 1 \\ \sqrt{\frac{1}{1+\text{St}} + \frac{1}{1+0.5\text{St}}} & \text{for } 1 \leq \text{St}, \end{cases} \quad (34)$$

where  $v_B, v_{r\text{pp}}, v_{\phi\text{pp}}, v_{z\text{pp}}$  and  $v_{\text{turb,pp}}$  are Brownian motion, radial drift difference, azimuthal drift difference, vertical settling difference, and turbulent velocity, respectively. Here, we assume that the relative velocity between particles can be represented by the velocity difference between two particles with  $t_s$  and  $0.5t_s$ , following Sato et al. (2016). Following EI17, we use the effective viscous parameter:

$$\alpha_D = \begin{cases} 0 & \text{for } \rho_{\text{pm}} < \rho_{\text{gm}} \\ 0.19 \left( \frac{\eta r}{H} \right) \min(\text{St}, 1) & \text{for } \rho_{\text{pm}} > \rho_{\text{gm}}, \end{cases} \quad (35)$$

where  $\eta$  is a dimensionless quantity that characterizes the pressure gradient of the gas disk and  $\rho_{\text{pm}}, \rho_{\text{gm}}$  are the dust and gas volume densities at the mid-plane of the disk. Here,  $\eta, \rho_{\text{pm}}$  and  $\rho_{\text{gm}}$  are given by

$$\eta = -\frac{1}{2} \frac{c_s^2}{r^2 \Omega^2} \left( \frac{\partial \log(\rho_{\text{gm}} T_m)}{\partial \log r} \right), \quad (36)$$

$$\rho_{\text{pm}} = \frac{\bar{f} \Sigma}{\sqrt{2\pi} z_p}, \quad (37)$$

$$\rho_{\text{gm}} = \frac{\Sigma}{\sqrt{2\pi} H}. \quad (38)$$

We adopt the turbulent Reynolds number  $\text{Re}$  from EI17:

$$\text{Re} = \frac{2\alpha_D c_s^2}{\Omega \lambda v_{\text{th}}}. \quad (39)$$

In our dust growth model, we do not consider the viscous stirring velocity  $v_{\text{vs}}$  considered in EI17 because it is orders of magnitude smaller than other velocity components when the dust is  $\mu\text{m}$  to  $\text{cm}$  size.

Using eq.(18) to eq.(39), we are able to integrate the ordinary differential eq.(17) by the Euler method. The time steps for the integration are:

$$\Delta t = \begin{cases} 10^{-1} \text{ yr} & \text{for } m_p > 10^{-4} \text{ g} \\ 10^{-3} \text{ yr} & \text{for } m_p < 10^{-4} \text{ g}. \end{cases} \quad (40)$$

Fig.2 shows the time evolution of the mass of dust particles for  $\dot{M} = 10^{-7.0} M_\odot/\text{yr}$ . Different curves in Fig.2 show the growth of dust particles at different radii in the disk. For all cases, the initial dust radius is set to  $0.1 \mu\text{m}$ . From Fig.2, we can calculate the timescale for a dust particle to grow to  $m_c$  at each radius  $r$  within the disk.

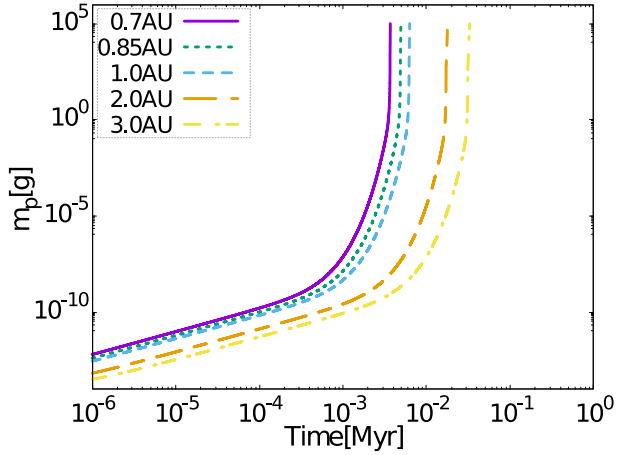


**Fig. 2.** The time evolution of  $m_p$ , starting from different initial distances from the central star. The accretion rate and the dust-to-gas fraction are  $\dot{M} = 10^{-7.0} M_\odot/\text{yr}$  and  $\bar{f} = \bar{f}_{\text{MMSN}}$ , respectively.

As we described in section 2.3.1, for simplicity, we assumed that dust particles grow through mutual collisions in situ, and once they have grown to  $m_c$ , they subsequently drift towards the Sun due to the gas drag. However, one might consider that these assumptions would be oversimplified for, at least, our models. We present the results of a growth model that accounts for dust particle migration, which show the validity of in situ growth of dust particles.

According to Weidenschilling (1977) and Nakagawa et al. (1986), the radial drift velocity of dust particles is given by

$$v_{\text{rp}} = \frac{2\text{St}}{1 + \text{St}^2} \eta r \Omega. \quad (41)$$

To consider dust particles migration as a part of the dust growth model, we need to integrate eq.(41) at the same time as integrating eq.(17) by using eq.(18) to eq.(40).

Figs. 3 and 4 show the evolution of the dust particle distance from the central star  $r_p$  as a function of time and

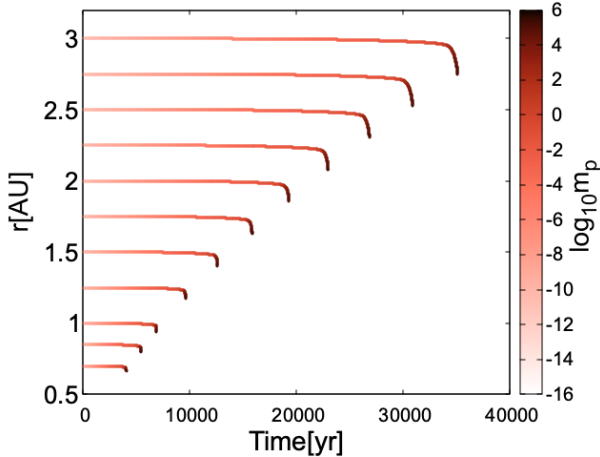


**Fig. 3.** The time evolution of the particle distance from the central star  $r_p$ , starting from different initial distances from the central star. The accretion rate and the dust-to-gas fraction are  $\dot{M} = 10^{-7.0} M_\odot/\text{yr}$  and  $\bar{f} = \bar{f}_{\text{MMSN}}$ , respectively. The color of the line indicates dust particle mass (color bar). Different curves in Fig.3 show the particles starting from different radii in the disk ranging from 0.7 to 3 AU.

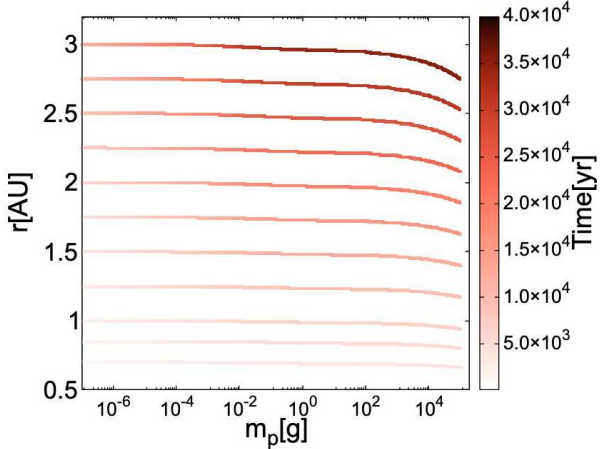


**Fig. 4.** Change in dust particle distance from central star  $r_p$  with an increase in dust particle mass, starting from different initial distances from the central star. The color of the line indicates time (color bar).

mass of the dust particle, respectively. In Fig.3, the line color represents the logarithmic mass of the dust particles. From these figures, it is seen that the radial migration of dust particles becomes pronounced when the dust particle mass exceeds  $\sim 10^2$  g, and the mass growth becomes much faster than radial migration.

### 2.3.3 The growth and migration timescales of dust particles

In section 2.3.2, we have seen that the evolution of the dust can be approximated as the two-stage phenomena. In the first stage, the dust grows at its radial position, until its mass reaches  $m_c$ . In the second stage, it migrates inward.

Using eqs.(17) and (41), we can write the particle mass growth timescale  $t_{\text{growth}}$  and the particle drift timescale

$t_{\text{drift}}$  as:

$$t_{\text{growth}} = \frac{m_p}{\frac{dm_p}{dt}} = \frac{m_p}{\pi a_p^2 \rho_p v_{\text{rel,pp}} \left( 1 + \frac{2Gm_p}{a_p v_{\text{rel,pp}}^2} \right)}, \quad (42)$$

$$t_{\text{drift}} = \frac{(r_p - r_{\text{in}})}{v_{rp}} = (r_p - r_{\text{in}}) \frac{1 + St^2}{2(St)\eta r \Omega}, \quad (43)$$

where  $r_p$  is the particle distance from the central star and  $r_{\text{in}}$  is the location of IDB given by eq.(12).

Fig.5 shows the ratio of  $t_{\text{growth}}$  to  $t_{\text{drift}}$  as a function of the dust particle mass  $m_p$ . The drift timescales are always

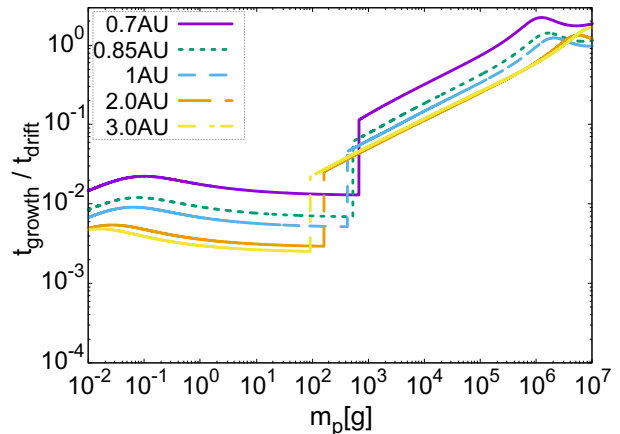


**Fig. 5.** The ratio of particle growth time scale to particle drift timescale at different radii in the disk. The accretion rate and the dust-to-gas fraction are  $\dot{M} = 10^{-7.0} M_\odot/\text{yr}$  and  $\bar{f} = \bar{f}_{\text{MMSN}}$ , respectively.

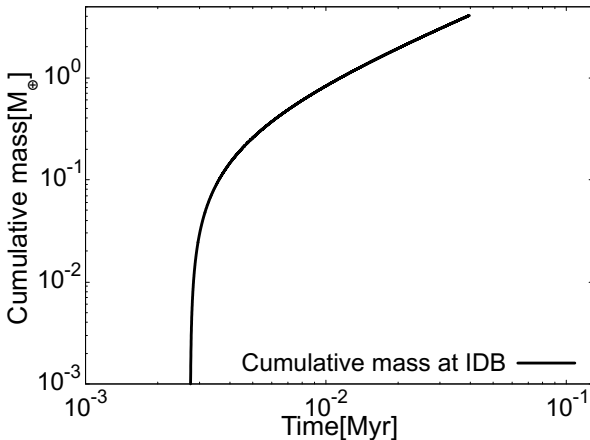
longer than the mass growth timescale, as far as the dust mass is less than  $\sim 10^5$  g, regardless of the distance from the Sun. Therefore, in this paper, we assume  $m_c = 10^5$  g, and regards dusts with masses larger than  $m_c$  as pebbles.

Fig.6 shows the cumulative mass reached to IDB as a function of time. In our model, we assume that all mass within WSZ eventually reaches IDB. Thus mass flow to IDB continues to time  $t = 3.7 \times 10^4$  yrs, with the inflow rate described as a function of time (see Appendix. 1 for more details).

### 2.4 Numerical methods

Using the model for the gas disk and that for the growth and migration of dust particles discussed in sections 2.2 and 2.3, we can determine the dust accretion timescale onto IDB. The accretion of dust onto IDB leads to the formation of planetesimals and planets in the vicinity of IDB. This phase of planet formation involves non-linear evolution, in which gravity becomes important. Therefore, we conduct  $N$ -body simulations from this phase.

In this subsection, we first provide a brief description of the  $N$ -body code GPLUM (Ishigaki et al. 2021) which we used in this study. Then, we describe how to incorporate



**Fig. 6.** The cumulative mass reached IDB as a function of time. The accretion rate and the dust-to-gas fraction are  $\dot{M} = 10^{-7.0} M_{\odot}/\text{yr}$  and  $f = f_{\text{MMSN}}$ , respectively.

the disk model and the dust growth model discussed in sections 2.2 and 2.3 into GPLUM. We describe how to set up the initial conditions for our  $N$ -body simulations.

#### 2.4.1 $N$ -body simulation code GPLUM

GPLUM (Ishigaki et al. 2021) is a parallel  $N$ -body simulation code for studying the formation of planetary systems. This code is developed using Framework for Developing Particle Simulator (FDPS) (Iwasawa et al. 2016; Namekata et al. 2018), a general-purpose, high-performance library for particle simulations. GPLUM is highly scalable under a parallel environment. Hereafter, we briefly describe the numerical scheme used in GPLUM.

GPLUM uses the particle-particle particle-tree ( $P^3T$ ) scheme, which is a hybrid integrator based on the splitting of the Hamiltonian (Oshino et al. 2011). The Hamiltonian of the system is divided into two parts depending on the cutoff radii of particles. The gravitational force between two particles is divided into short-range and long-range terms using the switching function scaled by the cutoff radius. The short-range part is called the hard part, while the long-range is called the soft part. The hard part consists of gravitational potential due to the central star and short-range interactions of particles. The time integration of the hard part is integrated by the fourth-order Hermite scheme (Makino 1991) with the individual timestep scheme (Aarseth 1963). When there are no neighbor particles within the cutoff radius, an analytic solution of the Kepler orbit around the central star is used. The soft part is calculated by using the Barnes-Hut tree scheme (Barnes & Hut 1986) available in FDPS. The hard and soft parts of the Hamiltonian used in the  $P^3T$  scheme are given by

$$H = H_{\text{Hard}} + H_{\text{Soft}}, \quad (44)$$

$$H_{\text{Hard}} = \sum_i \left[ \frac{|\mathbf{p}_i|^2}{2m_i} - \frac{GM_* m_i}{r_i} \right] - \sum_i \sum_{j > i} \frac{GM_* m_i}{r_{ij}} [1 - W(r_{ij}; r_{\text{out}})], \quad (45)$$

$$H_{\text{Soft}} = - \sum_i \sum_{j > i} \frac{GM_* m_i}{r_{ij}} W(r_{ij}; r_{\text{out}}), \quad (46)$$

$$r_{ij} = |\mathbf{r}_i - \mathbf{r}_j|, \quad (47)$$

where  $m_i$ ,  $\mathbf{p}_i$ ,  $\mathbf{r}_i$ ,  $r_{\text{out}}$  and  $W(r_{ij}; r_{\text{out}})$  are the mass, momentum, position of the  $i$ -th particle, the cutoff radius and the cutoff function for the Hamiltonian.

The cutoff radius for gravitational interactions between the  $i$ -th and  $j$ -th particles is set to be

$$r_{\text{out},ij} = \max(\tilde{R}_{\text{cut},0} r_{\text{Hill},i}, \tilde{R}_{\text{cut},1} v_{\text{ran},i} \Delta t, \tilde{R}_{\text{cut},0} r_{\text{Hill},j}, \tilde{R}_{\text{cut},1} v_{\text{ran},j} \Delta t), \quad (48)$$

where  $\tilde{R}_{\text{cut},0}$  and  $\tilde{R}_{\text{cut},1}$  are the parameters,  $r_{\text{Hill},i}$  and  $r_{\text{Hill},j}$  are the Hill radius, and  $v_{\text{ran},i}$  and  $v_{\text{ran},j}$  are the r.m.s random velocity for particles around  $i$ -th and  $j$ -th particles in GPLUM. Here, the random velocity is defined as the difference between its velocity and the Kepler velocity.

GPLUM uses the same cutoff function as Iwasawa et al. (2017) which is defined by

$$W(y; \gamma) = \begin{cases} \frac{7(\gamma^6 - 9\gamma^5 + 45\gamma^4 - 60\gamma^3 \ln \gamma - 45\gamma^2 + 9\gamma - 1)}{3(\gamma - 1)^7} y, & (y < \gamma), \\ f(y; \gamma) + [1 - f(1; \gamma)]y, & (\gamma \leq y < 1), \\ 1, & (1 \leq y), \end{cases} \quad (49)$$

where

$$\begin{aligned} f(y; \gamma) = & \{-10/3y^7 + 14(\gamma + 1)y^6 - 21(\gamma^2 + 3\gamma + 1)y^5 \\ & + [35(\gamma^3 + 9\gamma^2 + 9\gamma + 1)/3]y^4 \\ & - 70(\gamma^3 + 3\gamma^2 + \gamma)y^3 \\ & + 210(\gamma^3 + \gamma^2)y^2 - 140\gamma^3 y \ln y \\ & + (\gamma^7 - 7\gamma^6 + 21\gamma^5 - 35\gamma^4)\}/(\gamma - 1)^7. \end{aligned}$$

The cutoff function becomes unity when  $r_{ij}$  is longer than the cutoff radius for gravitational interactions between the  $i$ -th and  $j$ -th particles ( $r_{ij} > r_{\text{out},ij}$ ). Therefore, gravitational interactions of the hard part work only between particles with  $r_{ij} < r_{\text{out},ij}$ .

Using the individual cutoff method, GPLUM has made it possible to split gravitational interactions more efficiently compared to the original scheme that uses the “shared cutoff” radius for all particles. GPLUM can handle a large number of particles ( $N \sim 10^6$ ), a wide range in masses of particles, and a wide radial range (more than several AU) in simulations since it adopts the  $P^3T$  scheme

with the individual cutoff radius method.

#### 2.4.2 The prescription for our $N$ -body simulations

We aim to study the planet formation process in the vicinity of IDB, taking into account the in-situ growth of dust and dust migration discussed in section 2.3. Thus, in this section, we describe how to implement (1) the in-situ growth of dust, (2) the dust migration due to gas drag, and (3) the planet formation in the vicinity of IDB in GPLUM.

In our  $N$ -body simulations, we initially set particles with masses ranging from  $\sim 10^{22}$  g to  $\sim 10^{24}$  g, depending on the number of particles used in each simulation to match the solid surface density distribution of the disk (see section 2.4.3 and Appendix 1). Each of these particles represents a swarm of pebbles with a mass of  $m_c$ . We reproduce the in-situ growth of dust by maintaining the placed particles in-situ until they reach the timescale for the dust to grow up to  $m_c$ . To realize the in-situ orbital motion of particles, we need to suppress the effects of gravitational interaction between particles. Therefore, we set the mass of each particle to  $10^{14}$  g, which is the minimum mass that can be handled in GPLUM to minimize the effects of inter-particle gravitational interactions. Furthermore, the gas drag is disabled for each particle until it reaches the timescale for the dust mass to reach  $m_c$ .

Once the growth timescale is reached at each position within the disk, the gas drag force is applied to each particle to match the dust accretion timescale to reproduce mass accretion onto IDB (see Appendix 1). The gas drag force  $F_{\text{drag}}$  is given by Adachi et al. (1976) and Epstein (1924):

$$F_{\text{drag}} = \begin{cases} -\frac{4\pi}{3}\sqrt{\frac{8}{\pi}}\rho_g a_p^2 c_s v_{\text{rel},pp} & \text{For Epstein region } (a_p < \frac{9}{4}\lambda) \\ -6\pi\rho_g\nu a_p v_{\text{rel},pp} & \text{For Stokes region } (a_p > \frac{9}{4}\lambda). \end{cases} \quad (50)$$

Note that  $a_p$  in eq.(50) is the radius of a particle with mass  $m_c$ , since we are considering timescales for the accretion of pebble-sized objects within our simulations.

When a particle passes through IDB, the particle's radial migration is stopped by cutting off the gas drag force  $F_{\text{drag}}$ , and the mass is returned to the actual mass given in the initial condition in order to reproduce pebble accretion and accumulation onto IDB. This is equivalent to treating particles passing through IDB as having grown to planetesimals with the mass ( $\sim 10^{22-24}$  g) initially given to them due to the gravitational instability caused by dust concentration in the vicinity of IDB (e.g., Kato et al. 2010; Chatterjee & Tan 2014). In the same manner, when particles undergoing radial migration merge with particles that have already passed through IDB, they are processed to

return to the mass given in the initial condition before merging particles. Here we note that in our  $N$ -body simulations, we assume perfect accretion during particle collisions, neglecting the effects of fragmentation.

#### 2.4.3 Initial condition settings

In our simulations, we placed  $6 \times 10^4 \sim 1 \times 10^6$  particles of equal mass  $m_p$  in the radial range of  $r_{\text{in}} = 0.58$  AU to  $r_{\text{wsz}} = 3.28$  AU. Below, we provide a detailed description of the initial configuration of the dust particles.

The total dust mass in the radial range of  $r_{\text{in}}$  to  $r_{\text{wsz}}$  is given by

$$M_{\text{d,tot}} = \int_{r_{\text{in}}}^{r_{\text{wsz}}} 2\pi r \Sigma_p dr. \quad (51)$$

Using eq.(51),  $m_p$  is given by

$$m_p = \frac{M_{\text{d,tot}}}{N}. \quad (52)$$

The radial position of  $i$ -th particle,  $r_i$  is given by

$$M(r) = \int_{r_{i-1}}^{r_i} 2\pi r \Sigma_p dr = m_p, \quad (53)$$

where  $r_1 = r_{\text{in}}$ .

Table.1 summarizes our initial models. The surfaces of Table.1 show the names of the models, the dust-to-gas fraction  $\bar{f}_p$ , the initial total dust mass  $M_{\text{tot}}$ , the initial number of particles  $n_p$ , the initial mass of a particle  $m_{p,\text{init}}$ , and the mass of the largest particle at the end of the calculation  $m_{p,\text{max}}$ . Our reference model is N120Kc1, with  $N = 120k$ . For this model, the dust fraction normalized by MMSN value,  $f$ , is unity. We made three series of models starting from this reference model. In the first series, we vary  $f$  from 0.25 to 4. (N120Ka to Ke). In the second series, we vary the number of particles from 60k to 1M. In the third series, we added two models with all parameters the same as the reference model, but with different initial random seeds for angular coordinates of particles.

### 3 Results

In section 3.1, we summarize how planet formation proceeds in our model by showing the distribution of planets, the time evolution of mean and maximum masses of planets, and the cumulative mass distribution, using our fiducial model N120Kc1 as an example. In section 3.2, we compare simulation results for disks with different dust-to-gas fractions. In section 3.3, we investigate the particle number dependence of our simulations by using  $\bar{f} = \bar{f}_{\text{MMSN}}$  disk.

**Table 1.** List of models.

Name	$\bar{f}(\bar{f}_{\text{MMSN}})$	$M_{\text{tot}}(M_{\oplus})$	$N_p$	$m_{p,\text{init}}(M_{\oplus})$	$m_{p,\text{max}}(M_{\oplus})$
N120Kc1	1	4.07	$1.2 \times 10^5$	$3.3 \times 10^{-5}$	2.4
N120Ka	0.25	1.02	$1.2 \times 10^5$	$8.2 \times 10^{-6}$	0.49
N120Kb	0.5	2.03	$1.2 \times 10^5$	$4.1 \times 10^{-6}$	1.4
N120Kd	2	8.14	$1.2 \times 10^5$	$6.6 \times 10^{-5}$	5.4
N120Ke	4	16.27	$1.2 \times 10^5$	$1.3 \times 10^{-4}$	7.2
N60Kc	1	4.07	$6.0 \times 10^4$	$6.6 \times 10^{-5}$	2.6
N200Kc	1	4.07	$2.0 \times 10^5$	$2.0 \times 10^{-5}$	2.1
N1Mc	1	4.07	$1.0 \times 10^6$	$4.0 \times 10^{-6}$	2.5
N120Kc2	1	4.07	$1.2 \times 10^5$	$3.3 \times 10^{-5}$	2.7
N120Kc3	1	4.07	$1.2 \times 10^5$	$3.3 \times 10^{-5}$	2.5

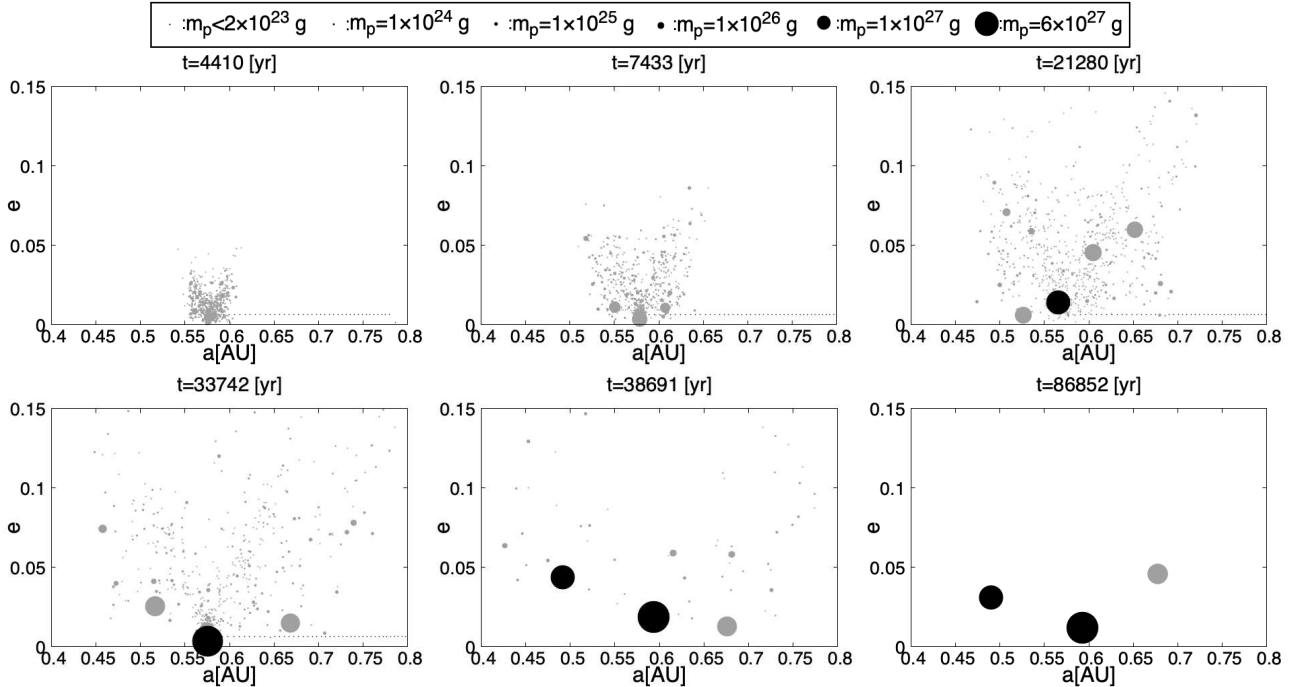


**Fig. 7.** Snapshots of planetary formations in model N120Kc1 arranged in chronological order from the upper left panel to the lower right panel in the  $a - e$  plane. Bodies above Earth mass are filled in black. The boxed legend shows the size of each representative mass and the filled circle size is proportional to  $m_p^{1/3}$ .

### 3.1 Planetary formation in our model

In this subsection, we first present the results of model N120Kc1 and give an overview of the planet formation process in our model.

#### 3.1.1 Planet formation process in Model N120Kc1

Fig.7 shows the distribution of particles in the  $a - e$  plane at several different epochs, where  $a$  is the semi-major axis and  $e$  is the eccentricity. The sizes of points are proportional to  $m_p^{1/3}$ , where  $m_p$  is the mass of a particle.

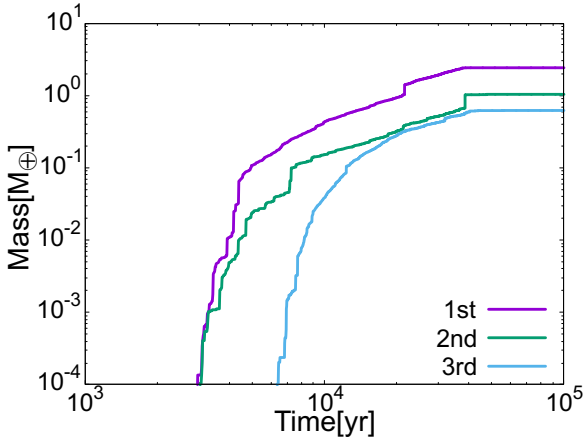
We can see that massive protoplanet forms very early on ( $t = 4410$  yrs). In this run, one massive planet continues to grow, but several less massive planets are formed and grow. At the end of the simulation, three planets remained.

Fig.8 shows the evolution of the masses of the three

most massive particles. The mass of the most massive planet jumps at  $t = 2.16 \times 10^4$  yrs. Here, planets with masses  $1.0 M_{\oplus}$  and  $0.36 M_{\oplus}$  collided. A similar jump also occurs at  $t = 3.9 \times 10^4$  yrs. Here, planets with masses  $0.66 M_{\oplus}$  and  $0.35 M_{\oplus}$  collided. These collisions can be regarded as Giant impacts, which might result in the formation of large moons.

Fig.9 shows the time evolution of the number of planetesimals and the average particle mass. The inflow of pebbles ends at  $t = 3.7 \times 10^4$  yrs. As we can see, while the pebble inflow continues, the total number of particles remains almost constant, and the average mass of particles grows nearly linearly. After the inflow stopped, the number of remaining particles decreases quickly and as a result the average particle mass goes up quickly.

These apparent changes simply reflect the fact that the pebble inflow stopped, and do not really imply the change in the growth mode. The late-phase evolution of the averaged particle mass is characterized by sudden increases, as a consequence of the giant impacts.



**Fig. 8.** The mass evolution of the three largest planets as a function of time in model N120Kc1.

### 3.1.2 Mass distribution of planetesimals and protoplanets

Fig.10 shows the cumulative mass distribution of planetesimals for the same epochs as in Fig.7. We can see that the evolution of the mass distribution in our model is very similar to that in the classical model starting from MMSN ignoring infalls driven by aerodynamic drag or type-I migration (Kokubo & Ida 1996; 1998, Makino et al. 1998). Initially, a power-law distribution develops, and then a few massive bodies start to grow, leaving out other less massive bodies. After the pebble infall stopped, these few massive bodies eat up the remaining small bodies.

This is because pebbles are continuously supplied from MSZ to IDB in our model. Thus, in our model, a few massive planets are formed while the pebble accretion is taking place. As a result, the formation time of Earth-like planets is much shorter compared to the prediction of the classic model, where Earth-like planets are formed through collisions between protoplanets after the planetesimals are cleared out.

### 3.2 The effect of the dust fraction

Fig.11 shows the evolution of the masses of three (or four) most massive bodies for runs with different initial dust fraction  $\bar{f}$ . In our model, the dust growth timescale depends on the dust number density and thus on  $\bar{f}$ , and is shorter for larger  $\bar{f}$ . Thus, the infall timescale is also shorter for larger  $\bar{f}$ . This is why the growth of massive

bodies is faster for larger  $\bar{f}$ .

We can see that, even though the mass inflow rate and total mass are changed by a factor of 16, the final outcomes are surprisingly similar. In all cases, three (or four in one case) massive bodies are formed and their masses are within a factor of five.

Fig.12 shows the semi-major axis and mass of massive bodies at the end of the simulation for models with different  $\bar{f}$ . We show the theoretical curve of the planet separation,

$$a = r_p \pm 5r_H, \quad (54)$$

where  $r_H$  is the Hill radius of the most massive body. We can see that the dependence of final separation to  $\bar{f}$  is due to the difference in the Hill radius.

Fig.13 shows the evolution of the semi-major axes of the massive bodies. We can see that the final separation of bodies is larger for larger  $\bar{f}$ . This is not surprising since the final mass of bodies is larger for  $\bar{f}$ .

Fig.14 shows the evolution of eccentricities of massive bodies. We can see that the eccentricities are generally small, even for the case of very massive planets. This is again quite different from the prediction of the classical model, which requires that the eccentricities of protoplanets grow large enough to allow mutual collisions. In our model, massive bodies are formed by pebble accretion, and there is no need to let them collide. As we have seen in section 3.1.1, there are a few collision events that can be regarded as giant impacts. However, even when such collisions take place, the eccentricities of bodies are not very large, simply because their radial separation is small.

### 3.3 The effect of the mass resolution

Fig.15 shows the evolution of the most massive plants (mass, semi-major axis, and eccentricity) for runs N60Kc to N1Mc, where we changed the total number of particles while keeping other parameters the same. We can see that the evolution is very similar for runs with widely different numbers of particles. The mass of the most massive planet is around  $2 M_\oplus$  for all runs, and that of the second and third massive planets are around  $1 M_\oplus$  and  $0.6 M_\oplus$ . The semi-major axes are around 0.58, 0.5, and 0.65 AU for the most massive, second (or third), and third (or second) most massive planets. Final eccentricities are less than 0.05 for all cases.

Since dust accumulates most at IDB where the pressure maximum is, it is typically considered that planets form most efficiently at IDB. Subsequently formed planets and surrounding planetesimals are scattered by the most massive planet and distributed in and out of the boundary.

**Table 2.** Summary of models with different dust to gas ratios  $\bar{f}$ .\*

Name	$\bar{f}(\bar{f}_{\text{MMSN}})$	$M_{1\text{st}}(M_{\oplus})$	$M_{2\text{nd}}(M_{\oplus})$	$M_{3\text{rd}}(M_{\oplus})$	$M_{4\text{th}}(M_{\oplus})$
N120Ka	0.25	0.49	0.25	0.23	0.03
N120Kb	0.5	1.4	0.37	0.25	-
N120Kc1	1	2.4	1.0	0.60	-
N120Kd	2	5.4	1.4	1.4	-
N120Ke	4	7.2	6.1	1.6	1.34

\* From left to right, the surfaces show the names of the models, the dust-to-gas fraction ( $\bar{f}_p$ ), the heaviest particle mass ( $M_{1\text{st}}$ ), the second heaviest particle mass ( $M_{2\text{nd}}$ ), the third heaviest particle mass ( $M_{3\text{rd}}$ ), the fourth heaviest particle mass ( $M_{4\text{rd}}$ ).

**Table 3.** Summary of models with different particle numbers  $N_p$ .\*

Name	$N_p$	$M_{1\text{st}}(M_{\oplus})$	$M_{2\text{nd}}(M_{\oplus})$	$M_{3\text{rd}}(M_{\oplus})$	$M_{4\text{th}}(M_{\oplus})$	$M_{5\text{th}}(M_{\oplus})$
N60Kc	$6 \times 10^4$	2.67	0.81	0.60	-	-
N120Kc1	$1.2 \times 10^5$	2.4	1.0	0.60	-	-
N200Kc	$2 \times 10^5$	2.1	0.72	0.62	0.54	0.09
N1Mc	$1 \times 10^6$	2.5	0.92	0.62	-	-

\* From left to right, the surfaces show the names of the models, the initial number of particles ( $N_p$ ), the heaviest particle mass ( $M_{1\text{st}}$ ), the second heaviest particle mass ( $M_{2\text{nd}}$ ), the third heaviest particle mass ( $M_{3\text{rd}}$ ), the fourth heaviest particle mass ( $M_{4\text{rd}}$ ), the fifth heaviest particle mass ( $M_{5\text{rd}}$ ).

Cai et al. (2022) also studied planet formation in the pebble ring located in IDB, and their study also found that the most massive planet tended to form in the center of the ring compared to the location of the second massive planet.

We can conclude that our result does not depend on the mass of “pebbles”, even though our “pebbles” are still many orders of magnitude more massive than real ones.

## 4 Discussion

In this section, we discuss the relation between our model and those in recent studies in which the radial structure of the protoplanetary disk is taken into account.

Ogihara et al. (2018) considered both MRI-active and MRI-inactive disk structures in which the surface density is flat, or increasing outward a certain radius. In such disk profiles, the Type I migration is suppressed. In such a disk, it is possible that planet formation occurs in a wide area around 1 AU (Ogihara et al. 2018). They have simulated the late stage of planet formation from planetary embryos. They used the same initial condition as Hansen (2009) assuming a uniform solid surface density ranging from 0.7–1 AU with 400 bodies of equal mass. Each body has a mass of  $0.005 M_{\oplus}$ , resulting in a total mass of  $2 M_{\oplus}$ . They showed that Earth-like planets are formed through collisions of planetary embryos, with a formation timescale of 100 Myr.

In contrast to Ogihara et al. (2018), we conducted  $N$ -body simulation to directly simulate the formation and

growth of planetary embryos through pebble accretion. The notable difference between our results and Ogihara et al. (2018) is the planet formation timescale. In our simulation, Earth-like planets are formed within 0.1 Myr. This is because, in our model, the continuous supply of pebbles from the outer disk allows the efficient growth of planetesimals through collisions with both planetesimals and pebbles.

Jiang & Ormel (2023) studied the formation and evolution of planetesimals in a clumpy ring and a ring induced by a permanent pressure bump by conducting  $N$ -body simulations. Lau et al. (2022) also investigated planetesimals growth and their migration within a pressure bump. In both studies, they focused on planet formation at a pressure bump located at a distance of 75 AU from the central star motivated by observations (e.g., Andrews et al. 2018). In addition, Lau et al. (2022) studied the planet formation process at a pressure bump located at a distance of 10 AU from the central star. In our study, we are interested in the planet formation process around 1 AU. Thus, it is difficult to compare the result of their work and our work directly.

In our study, planetesimals formed early on the high-mass end of the cumulative mass distribution grow rapidly, leaving out other less massive bodies by pebble accretion (Figs. 10). These few massive bodies continue to grow efficiently until the pebble infall phase ends. During the pebble infall phase, the total number of particles in the vicinity of IDB remains nearly constant, despite the continuous supply of dust particles. This indicates that few massive bodies eat the infalling particles while stirring a

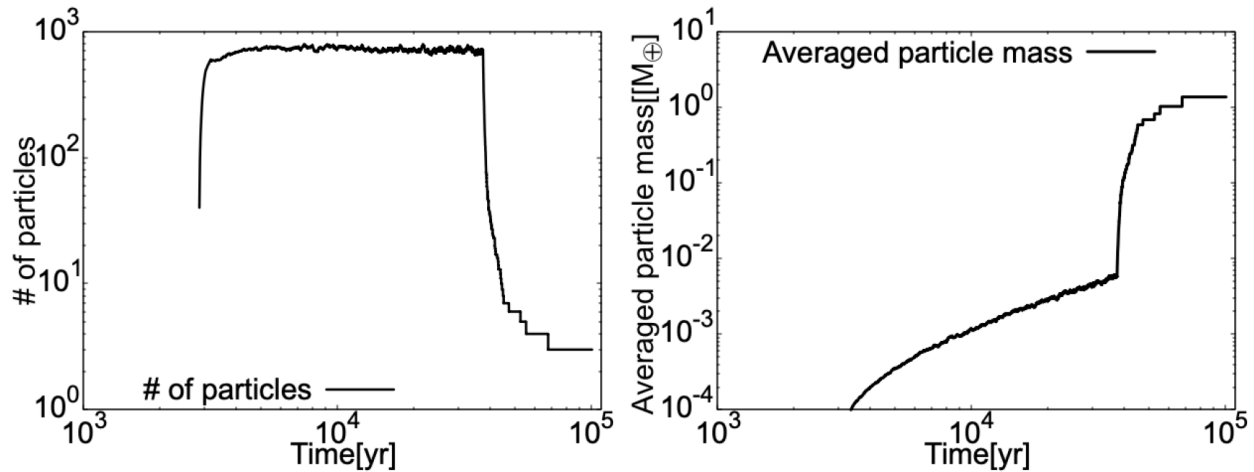


**Fig. 9.** The number of particles that are above the planetesimal mass (left) and the average mass of particles (right) as a function of time.

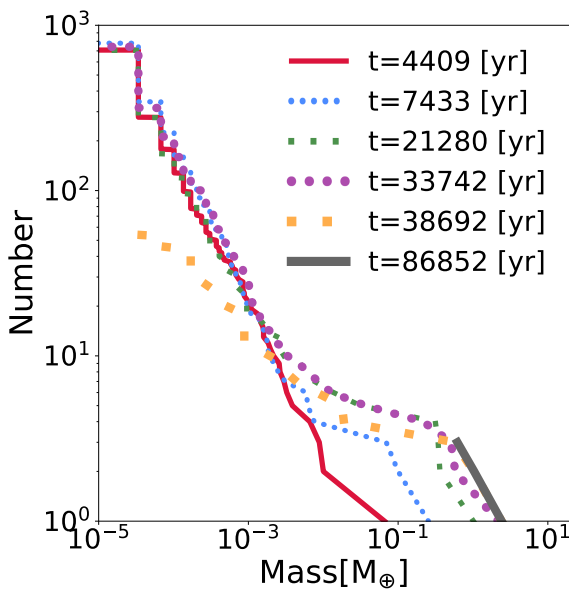


**Fig. 10.** The time evolution of the cumulative mass distribution in model N120Kc1 (Note that particles that have not yet accreted to IDB are ignored)

certain number of small bodies and preventing the growth of those small ones left behind. After the end of the pebble infall phase, these few massive bodies eat up all remaining small bodies, and only a small number of massive bodies are formed. The orbital separations between these few massive bodies are more than  $5 r_H$  at the end of our simulations (Fig.12). This is because they undergo scattering between planets (Kokubo & Ida 1995).

## 5 Summary and Conclusion

In our study, we simulated the formation of a solar-system-like terrestrial planetary system with pebble accretion and

particle coalescence by performing  $N$ -body simulations with a large number of particles ( $6 \times 10^4$  to  $1 \times 10^6$  particles).

We started from a protoplanetary disk inferred from recent standard understanding, which has dead zone in the radial range of around 0.5-3 AU. We followed the growth and inward migration of dust in this region and study how they form planets at the inner dead zone boundary (IDB) through  $N$ -body simulation. Our findings are summarized as follows.

1. We found that planet formation at IDB is quite efficient. Independent of the inflow rate of the pebbles, massive planets are formed by the end of the pebble accretion phase. Runaway growth leads to the formation of three to four massive planets, and their total mass becomes comparable to the total mass inflow rather early.
2. Our results do not depend on the mass resolution of our  $N$ -body simulation. Therefore, we can expect that a similar formation process take place even for real pebbles with much smaller mass, as far as the total inflow mass is similar.
3. Since the planets grow mainly through pebble accretion, their final eccentricities are relatively small. Even so, there are several collision events that can be regarded as giant impacts.

Based on our findings, we can conclude that there is a possibility for the formation of planetary systems resembling the Solar System within radially structured protoplanetary disks. Recent observational studies using the Atacama Large Millimeter/sub-millimeter Array (ALMA) have revealed the presence of dust ring-gap structures even within young protoplanetary disks, approximately the age of 1 Myr after the central star has formed (e.g., Dullemond et al. 2018). A more recent study has suggested that plane-

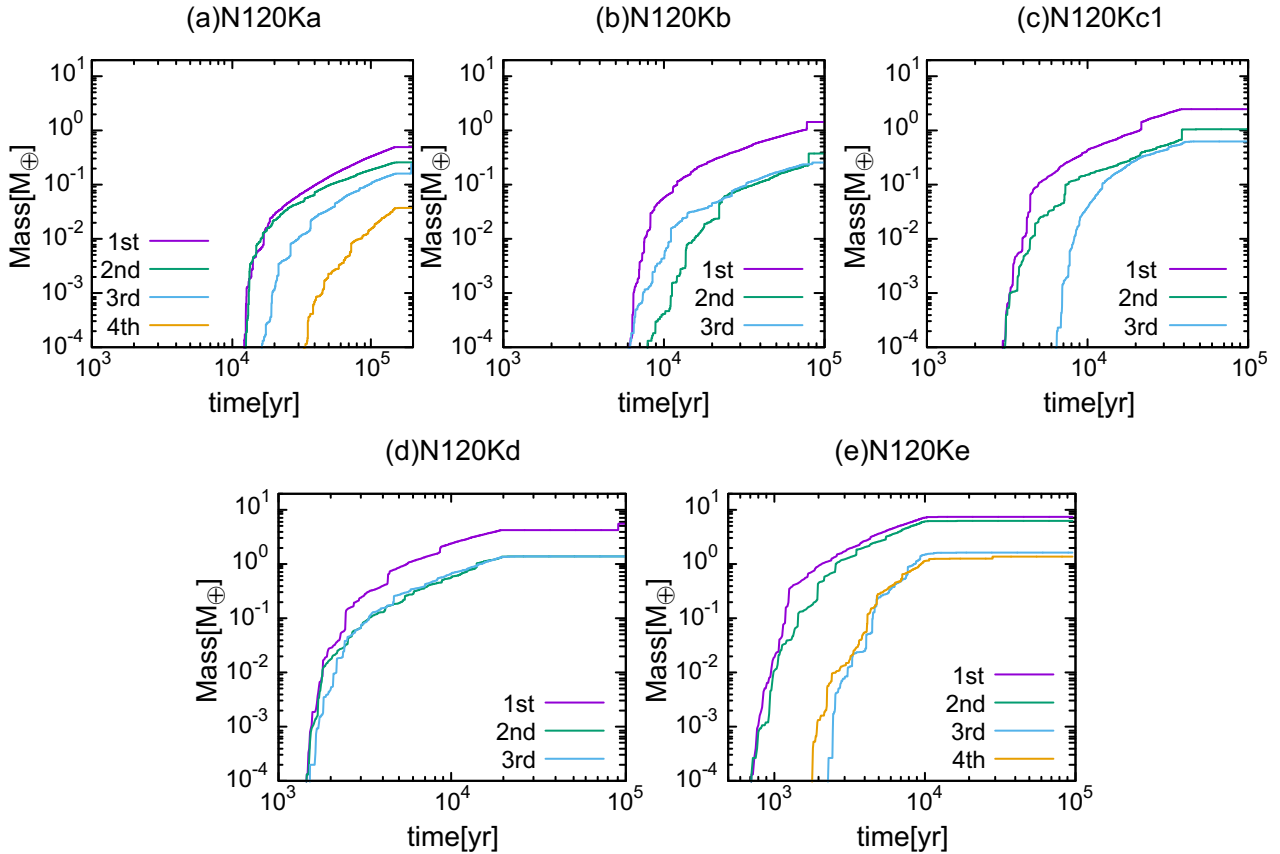


**Fig. 11.** Time evolution of particles' mass for each dust-to-gas fraction in the  $m_p - t$  plane. Results are shown for disks of  $\bar{f} = (0.25, 0.5, 1, 2, 4) \times \bar{f}_{\text{MMSN}}$  in order from upper left to the lower right in the figure, respectively.

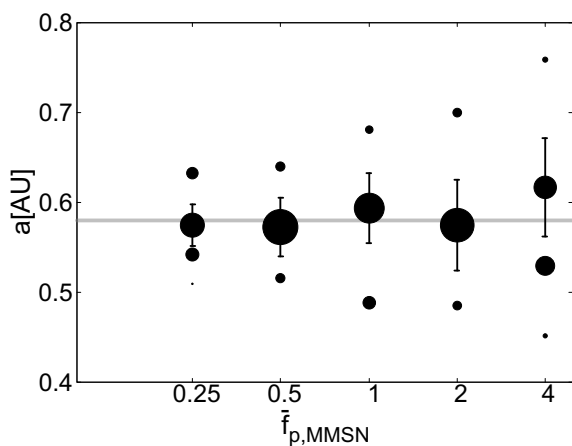


**Fig. 12.** The semi-major axis and mass of massive bodies at the end of the simulation for models with different  $\bar{f}$ . The size of each dot represents the planet mass normalized by the total dust mass for each  $\bar{f}$ . The lines from the center of the most massive planets to both sides have the length of  $5r_{\text{H}}$ . The grey line represents inner dead zone boundary ( $\sim 0.58\text{AU}$ ). See table 2 for detailed values of the planetary masses formed at each value of  $\bar{f}$ .

tary system formation proceeds rapidly with the timescale of 0.1 - 1 Myr after the central star has formed (Ohashi et al. 2023). Our results may provide theoretical support for the efficient formation of planetary systems within such dust rings.

The main limitation of our current model is that the structure of the gas disk is oversimplified. We essentially placed a sharp cutoff of the gas disk at IDB. As suggested by many recent works (e.g. Suzuki et al. 2010; 2016), the inner boundary of the gas disk might not be a sharp one but a more smooth transition driven by magnetic disk wind. It is also important to take into account the effect of the Type-I migration (Jiang & Ormel 2023; Jang et al. 2022). We will extend our work to study these effects.

## Acknowledgments

We thank the anonymous referee for providing useful feedback that contributed to the improvement of our paper. This work was supported by MEXT as “Program for Promoting

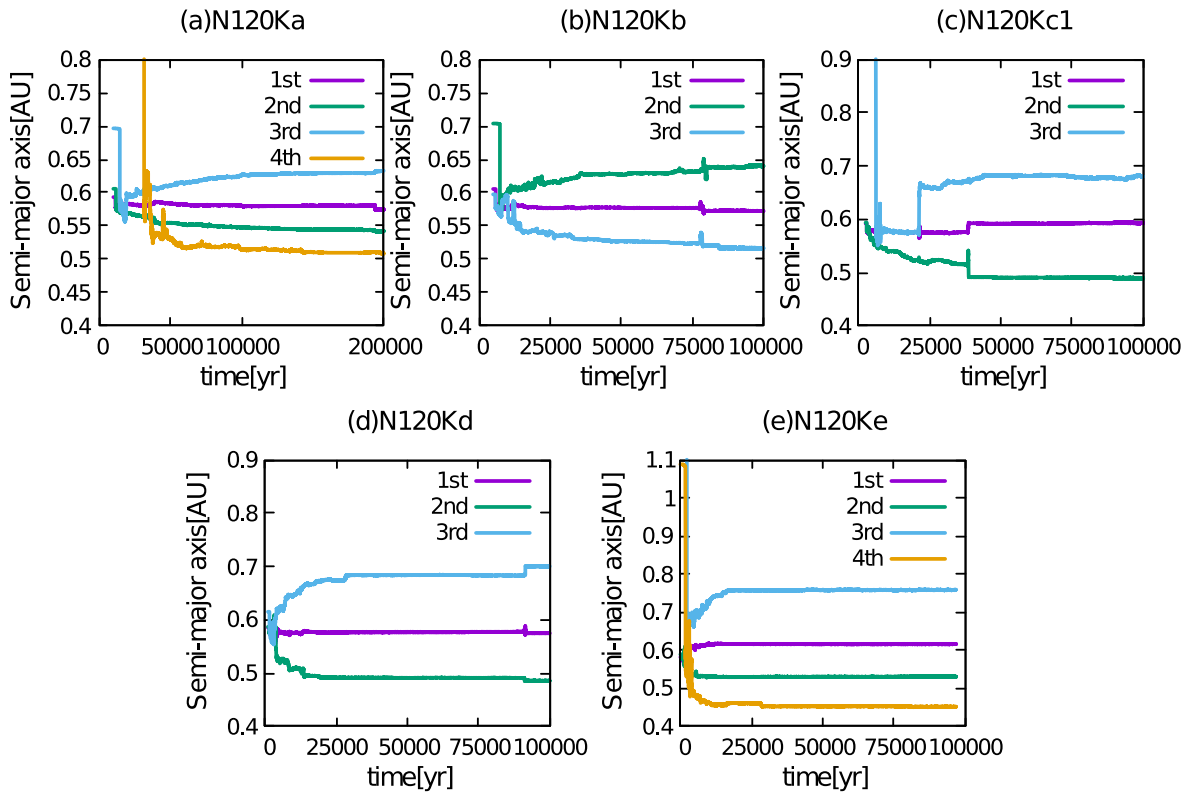


**Fig. 13.** Time evolution of particles' semi-major axis for each dust-to-gas fraction in the  $a - t$  plane. Results are shown for disks of  $\bar{f} = (0.25, 0.5, 1, 2, 4) \times \bar{f}_{\text{MMSN}}$  in order from upper left to the lower right in the figure, respectively.

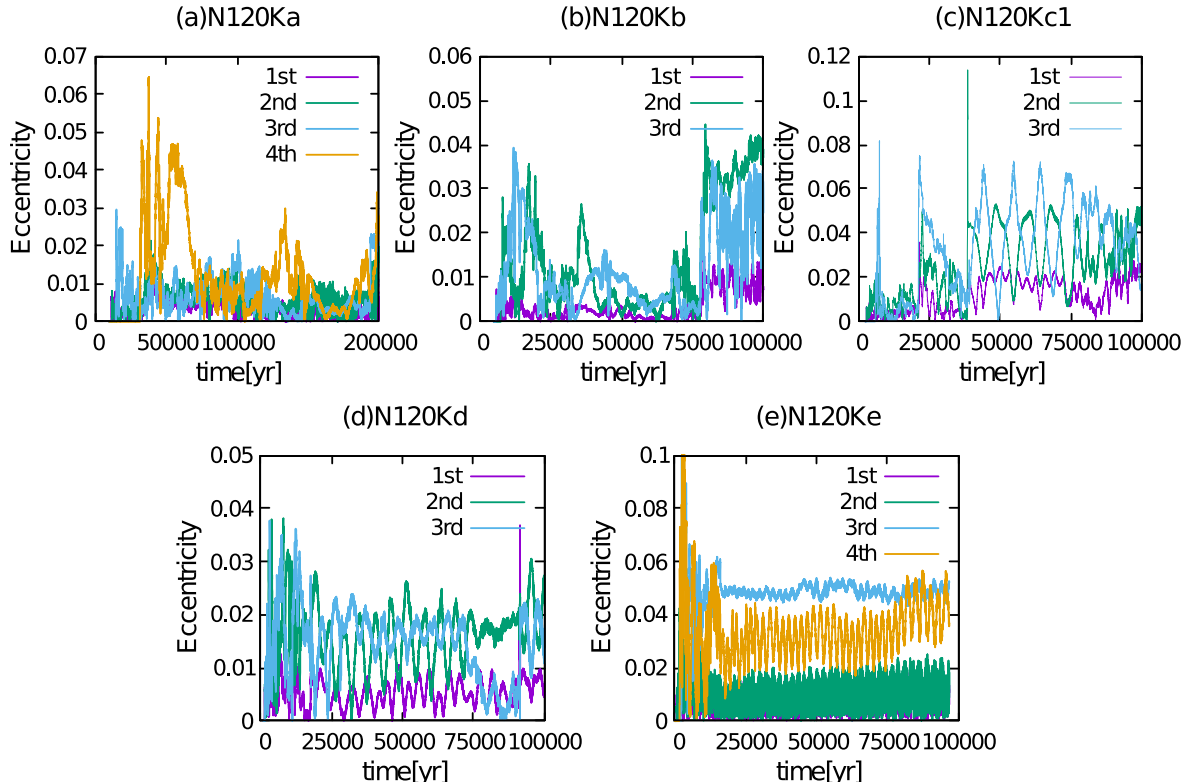


**Fig. 14.** Time evolution of particles' eccentricity for each dust-to-gas fraction in the  $e - t$  plane. Results are shown for disks of  $\bar{f} = (0.25, 0.5, 1, 2, 4) \times \bar{f}_{\text{MMSN}}$  in order from upper left to the lower right in the figure, respectively.

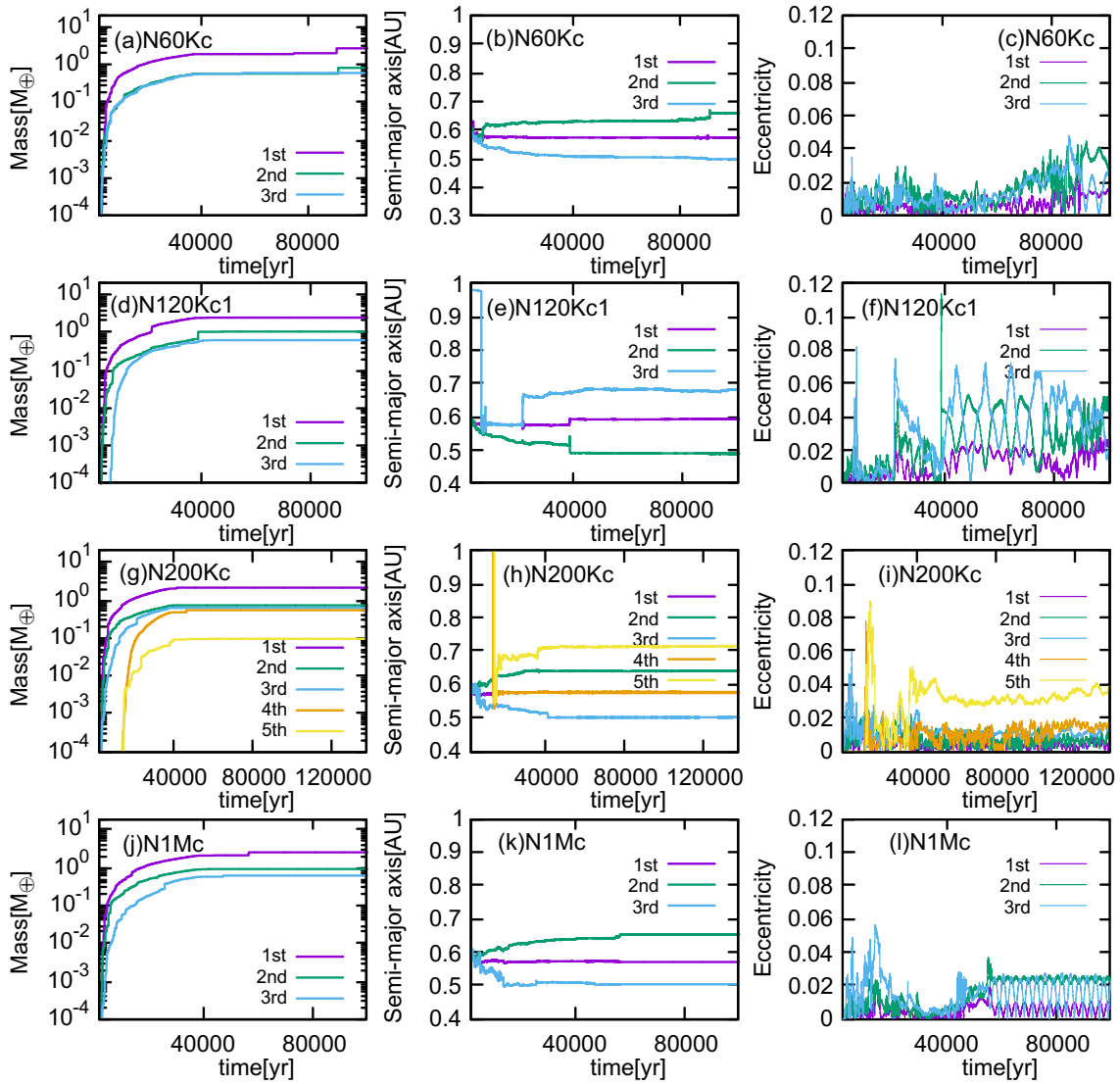


**Fig. 15.** The simulation results for the  $6 \times 10^4$ ,  $1.2 \times 10^5$ ,  $2 \times 10^5$ , and  $1 \times 10^6$  particle systems in order from the top row to the bottom row. The left, middle and right surfaces are the results of the time evolution of the particle mass, semi-major axis, and eccentricity, respectively.

Researches on the Supercomputer Fugaku” (Structure and Evolution of the Universe Unraveled by Fusion of Simulation and AI; Grant Number JPMXP1020230406) and used computational resources of supercomputer Fugaku provided by the RIKEN Center for Computational Science (Project ID: hp230204). The simulations in this paper were also carried out on a Cray XC50 system at the Centre for Computational Astrophysics (CfCA) of the National Astronomical Observatory of Japan (NAOJ).

## Appendix 1 Mass flux onto IDB in our *N*-body simulation

In our model, we assumed that dust particles grow in situ and begin to drift toward the Sun once their mass reaches

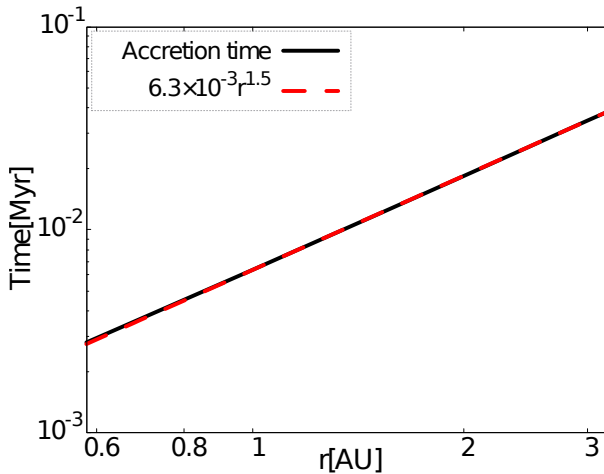
$m_c$ . This means that the accretion time to IDB from the beginning of the simulation,  $t_{\text{acc}}$ , consists of the sum of the two timescales:

$$t_{\text{acc}}(r) = t_{\text{grow}}(r) + t_{\text{drift}}(r), \quad (\text{A1})$$

where  $r$  is the initial position of a dust particle,  $t_{\text{grow}}$  is the time it takes for a dust particle to grow to  $m_c$  and  $t_{\text{drift}}$  is the particle drift timescale given by eq.(43).

Fig.16 shows the accretion time as a function of the dust particle position  $r$ . We draw a fitting line with a simple power law form (red dashed line) in the figure as well as the numerical simulation (black line). The function form of the accretion timescale is

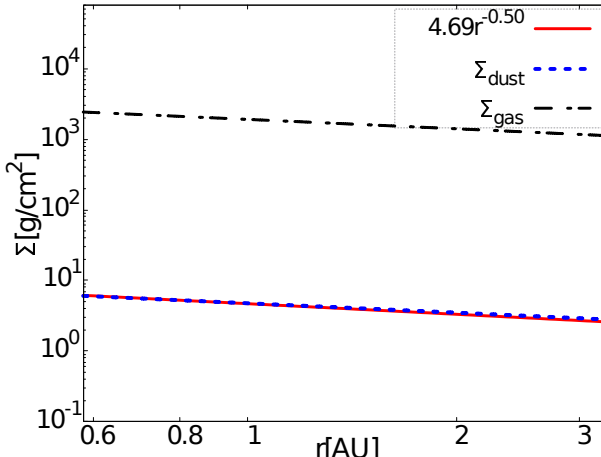
$$t_{\text{acc}}(r) = 6.3 \times 10^{-3} r^{1.5} \text{ Myr.} \quad (\text{A2})$$



**Fig. 16.** The accretion time  $t_{\text{acc}}$  at different radii in the disk (black line). The approximation of  $t_{\text{acc}}$  as a function of the disk radius (red dashed line). The accretion rate and the dust-to-gas fraction are  $\dot{M} = 10^{-7.0} M_{\odot}/\text{yr}$  and  $\bar{f} = \bar{f}_{\text{MMSN}}$ , respectively.

By solving this equation for  $r$ , we can obtain the distance where the dust particles just reach IDB at a given time.

In our  $N$ -body simulations, we reproduced the accretion of dust particles onto IDB in accordance with  $t_{\text{acc}}$  given by eq.(A2). To verify that our  $N$ -body simulation accurately reproduces the mass flux, we need to compare the analytically derived mass flux using  $t_{\text{acc}}$  with our  $N$ -body simulation result. In the following, we briefly describe a method for determining the mass flux analytically and compare it with our  $N$ -body simulation result.



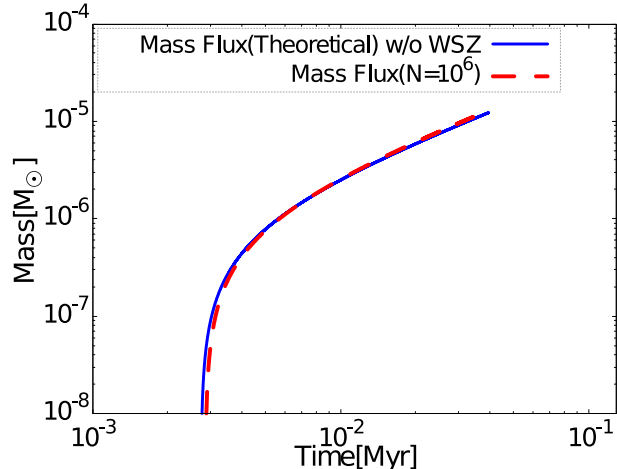
**Fig. 17.** The radial profile of the surface density of the dust (blue dotted line) and gas (black dash-dotted line) for  $\dot{M} = 10^{-7.0} M_{\odot}/\text{yr}$  ranging from  $r_{\text{in}}$  to  $r_{\text{WSZ}}$ . The approximation of  $\Sigma_{\text{dust}}$  as a function of the disk radius (red line).

Fig.17 shows the result of  $\Sigma_{\text{dust}}$  and  $\Sigma_{\text{gas}}$  for  $\dot{M} = 10^{-7.0} M_{\odot}/\text{yr}$  ranging from  $r_{\text{in}} = 0.58$  AU to  $r_{\text{WSZ}} = 3.28$  AU. Here we note that  $r_{\text{in}}$  and  $r_{\text{WSZ}}$  represent the inner boundaries of the dead zone and water sublimation zone,

respectively. According to Fig.17, the dust surface density  $\Sigma_{\text{dust}}$  in MSZ can be approximated as a power function of distance  $r$ , yielding the following functional form:

$$\Sigma_{\text{dust}} = \bar{f} \Sigma_{\text{gas}} = 4.69 \left( \frac{\bar{f}}{\bar{f}_{\text{MMSN}}} \right) r^{-0.5} \text{ g cm}^{-2}. \quad (\text{A3})$$

Solving eq.(A2) for  $r$ , we can determine how far dust particles accrete at a given time (here we denote  $r$  as  $r_{\text{acc}}$ ). By substituting  $r_{\text{acc}}$  into eq.(A3) and integrating it over time, we can calculate how much dust has accreted onto IDB by a certain time. Here, we call it “theoretical mass flux”.



**Fig. 18.** Comparison of theoretical mass flux with the  $N$ -body simulation result. The vertical axis represents the total mass flux onto IDB up to a certain time. The theoretical values (blue line) and the model for  $1 \times 10^6$  particles (red dashed line).

In Fig.18, we show the results for the theoretical mass flux (blue line) and the model for  $1 \times 10^6$  particles (red dashed line) with  $\bar{f} = \bar{f}_{\text{MMSN}}$  disk. Fig.18 supports that our  $N$ -body simulations successfully reproduce mass inflow into IDB with high accuracy.

## Appendix 2 Energy error in our $N$ -body simulation

In our model, there are sudden mass changes in particles, resulting in non-mechanical energy changes. It is, thus, necessary to count these energy changes to see the total energy errors in our simulations. In our simulation code, the change of mass takes place at the end of the hard part when the particle passes through IDB or collides with another particle. By keeping the energies before the mass change, we can count the total energy change induced by this operation.

The energy change due to the mass changes of particles, i.e., the non-mechanical energy change, is calculated as the summation of the increase of the kinetic energy and

gravitational energy of the particle due to the change in mass. The non-mechanical energy change at a step is as follows:

$$\Delta E_{\text{n.m.}} = \sum_i [\epsilon_{0,i} + \epsilon_{1,i} + \epsilon_{2,i} + \epsilon_{3,i}], \quad (\text{A4})$$

$$\epsilon_{0,i} = \frac{1}{2} \Delta m_i v_p^2, \quad (\text{A5})$$

$$\epsilon_{1,i} = -G \Delta m_i \sum_{k \in N_i} m_k \left[ \frac{W(r_{ij}; r_{\text{out},ij})}{r_{ik}} \right] \quad (\text{A6})$$

$$\epsilon_{2,i} = -\frac{G \Delta m_i M_*}{r_i}, \quad (\text{A7})$$

$$\epsilon_{3,i} = \Delta m_i \phi_{\text{soft},i}, \quad (\text{A8})$$

where  $\Delta m_i$  is the change in mass of  $i$ -th particle ( $m_{\text{new}} = m_{\text{old}} + \Delta m_i$ ),  $W(r_{ij}; r_{\text{out},ij})$  is the cutoff function used in P<sup>3</sup>T,  $N_i$  is the number of neighbor particles of the  $i$ -th particle,  $\phi_{\text{soft},i}$  is the soft part of the gravitational potential for  $i$ -th particle. The four terms of eq. (A4) represent the energy changes of the kinetic energy, the gravitational potential energy in the short-range interactions, the gravitational potential energy with respect to the central star, and the gravitational potential energy in the long-range interactions, respectively. Fig.19 shows the relative energy

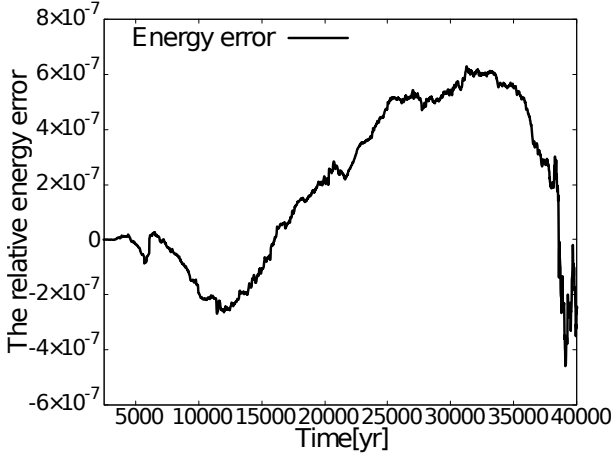


**Fig. 19.** The time evolution of the relative energy error for N120Kc1. The relative energy error is given as  $(E_{\text{now}} - E_{\text{initial}} - E_{\text{n.m.}})/E_{\text{now}}$ .

error of N120Kc1 involving the energy correction due to mass changes as a function of time. From this figure, we can confirm that the correction of the sudden mass changes functioned properly. Note that Fig.19 shows only the first  $4 \times 10^4$  yr since the accretion stops around the epoch and there is no need to correct induced by the mass changes after this epoch.

## References

- Aarseth, S. J. 1963, MNRAS, 126, 223
- Adachi, I., Hayashi, C., & Nakazawa, K. 1976, Progress of Theoretical Physics, 56, 1756
- Alessi, M., & Pudritz, R. E. 2018, MNRAS, 478, 2599
- Andrews, S. M., Huang, J., Pérez, L. M., et al. 2018, ApJL, 869, L41
- Armitage, P. J. 2011, ARA&A, 49, 195
- . 2020, Astrophysics of planet formation, Second Edition (Cambridge University Press)
- Bai, X.-N., & Stone, J. M. 2013, ApJ, 769, 76
- Balbus, S. A., & Hawley, J. F. 1991, ApJ, 376, 214
- Barnes, J., & Hut, P. 1986, Nature, 324, 446
- Birnstiel, T., Klahr, H., & Ercolano, B. 2012, A&A, 539, A148
- Cai, M. X., Tan, J. C., & Portegies Zwart, S. 2022, MNRAS, 510, 5486
- Chatterjee, S., & Tan, J. C. 2014, ApJ, 780, 53
- Coleman, G. A. L., & Nelson, R. P. 2014, Monthly Notices of the Royal Astronomical Society, 445, 479
- Coleman, G. A. L., & Nelson, R. P. 2016, MNRAS, 460, 2779
- Davis, S. W., Stone, J. M., & Pessah, M. E. 2010, ApJ, 713, 52
- Dullemond, C. P., Birnstiel, T., Huang, J., et al. 2018, ApJL, 869, L46
- Ebisuzaki, T., & Imaeda, Y. 2017, New Astronomy, 54, 7
- Epstein, P. S. 1924, Phys. Rev., 23, 710
- Hansen, B. M. S. 2009, ApJ, 703, 1131
- Hayashi, C. 1981, Progress of Theoretical Physics Supplement, 70, 35
- Hayashi, C., Nakazawa, K., & Nakagawa, Y. 1985, in Protostars and Planets II, ed. D. C. Black & M. S. Matthews, 1100–1153
- Hubeny, I. 1990, ApJ, 351, 632
- Hyodo, R., Ida, S., & Guillot, T. 2021, A&A, 645, L9
- . 2022, A&A, 660, A117
- Ida, S., & Lin, D. N. C. 2008, ApJ, 673, 487
- Ida, S., & Makino, J. 1993, Icarus, 106, 210
- Ishigaki, Y., Kominami, J., Makino, J., Fujimoto, M., & Iwasawa, M. 2021, PASJ, 73, 660
- Iwasawa, M., Oshino, S., Fujii, M. S., & Hori, Y. 2017, PASJ, 69, 81
- Iwasawa, M., Tanikawa, A., Hosono, N., et al. 2016, PASJ, 68, 54
- Jang, H., Liu, B., & Johansen, A. 2022, A&A, 664, A86
- Jiang, H., & Ormel, C. W. 2023, MNRAS, 518, 3877
- Johansen, A., & Lambrechts, M. 2017, Annual Review of Earth and Planetary Sciences, 45, 359
- Kato, M. T., Fujimoto, M., & Ida, S. 2010, ApJ, 714, 1155
- Kokubo, E., & Ida, S. 1995, Icarus, 114, 247
- . 1996, Icarus, 123, 180
- . 1998, Icarus, 131, 171
- Lambrechts, M., & Johansen, A. 2012, A&A, 544, A32
- . 2014, A&A, 572, A107
- Lau, T. C. H., Dražkowska, J., Stammle, S. M., Birnstiel, T., & Dullemond, C. P. 2022, A&A, 668, A170
- Lyra, W., Johansen, A., Zsom, A., Klahr, H., & Piskunov, N. 2009, A&A, 497, 869
- Makino, J. 1991, ApJ, 369, 200
- Makino, J., Fukushige, T., Funato, Y., & Kokubo, E. 1998, NewA, 3, 411

- Matsumura, S., Brasser, R., & Ida, S. 2017, A&A, 607, A67  
—. 2021, A&A, 650, A116
- Mizuno, H. 1980, Progress of Theoretical Physics, 64, 544
- Muto, T., Tsukagoshi, T., Momose, M., et al. 2015, PASJ, 67, 122
- Nakagawa, Y., Sekiya, M., & Hayashi, C. 1986, Icarus, 67, 375
- Namekata, D., Iwasawa, M., Nitadori, K., et al. 2018, PASJ, 70, 70
- Ogihara, M., Kokubo, E., Suzuki, T. K., & Morbidelli, A. 2018, A&A, 612, L5
- Ohashi, N., Tobin, J. J., Jørgensen, J. K., et al. 2023, ApJ, 951, 8
- Ormel, C. W., & Cuzzi, J. N. 2007, A&A, 466, 413
- Oshino, S., Funato, Y., & Makino, J. 2011, PASJ, 63, 881
- Sato, T., Okuzumi, S., & Ida, S. 2016, A&A, 589, A15
- Shakura, N. I., & Sunyaev, R. A. 1973, A&A, 24, 337
- Stepinski, T. F. 1998, Icarus, 132, 100
- Suzuki, T. K., Muto, T., & Inutsuka, S.-i. 2010, ApJ, 718, 1289
- Suzuki, T. K., Ogihara, M., Morbidelli, A., Crida, A., & Guillot, T. 2016, A&A, 596, A74
- Tanaka, H., Takeuchi, T., & Ward, W. R. 2002, ApJ, 565, 1257
- Ward, W. R. 1986, Icarus, 67, 164
- Weidenschilling, S. J. 1977, MNRAS, 180, 57
- Wetherill, G. W., & Stewart, G. R. 1989, Icarus, 77, 330
- Youdin, A., & Johansen, A. 2007, ApJ, 662, 613